



RESEARCH ARTICLE

WILEY

Conversion of explicit microplane model with boundaries to a constitutive subroutine for implicit finite element programs

Hoang T. Nguyen¹ | Ferhun C. Caner² | Zdeněk P. Bažant³

¹Theoretical and Applied Mechanics,
Northwestern University, Evanston,
Illinois, USA

²Institut de Tècniques Energètiques and
Departament de Ciència i Enginyeria de
Materials, Universitat Politècnica de
Catalunya, Barcelona, Spain

³Civil and Mechanical Engineering and
Materials Science, Northwestern
University, Evanston, Illinois, USA

Correspondence

Zdeněk P. Bažant, Civil and Mechanical
Engineering and Materials Science,
Northwestern University, 2145 Sheridan
Road, CEE/A135, Evanston, IL 60208,
USA.
Email: z-bazant@northwestern.edu

Funding information

National Science Foundation,
Grant/Award Number: CMMI-202964

Abstract

Whereas various simplistic microplane models of limited applicability, defined by stress-strain curves on the microplane, can function as either explicit or implicit, the explicit-to-implicit conversion of realistic versatile microplane models for plain or fiber-reinforced concrete, shale and composites has remained a challenge for quarter century. The reason is that these realistic models use microplane stress-strain boundaries defined by inequalities. Here, we show how the conversion can be easily achieved on the microplane level and then transferred to a tangent stiffness tensor or an inelastic stiffness tensor to be used in Newton–Raphson iterations within a loading step. To ensure convergence, a minor adjustment in the M7 algorithm is introduced to achieve continuity. Power-law convergence, almost quadratic in most cases, is also demonstrated. Seven examples of crack-band finite element simulations of challenging laboratory tests document nearly identical implicit and explicit results, as well as good match of test data. Three of them, including the vertex effect in compression-torsion tests, pure Mode II shear fracture, and the “gap test” of the crack-parallel compression effect on Mode I load-deflection curve, have not been reproduced by other models before. The coding of implicit M7 subroutine, usable in, for example, UMAT of ABAQUS, is posted for a free download.

KEY WORDS

constitutive models, damage modeling, gap test, mixed-mode fracture, quasibrittle materials, vertex effect

1 | INTRODUCTION

Since 1983¹ and until 1996, all of the microplane damage constitutive models were either implicit^{2–9} or easily converted to implicit form by differentiation of microplane stress-strain curve. They provided the tangent stiffness tensor of the material for implicit finite element (FE) program, and could serve as the user-defined material subroutine, for example, UMAT in ABAQUS. While the development of various implicit microplane models has continued, it gradually transpired from test data fitting that a broader range of behavior of concrete and other quasibrittle materials could be captured by an explicit microplane model with many inequalities, representing the stress-strain boundaries for various orientation, analogous to strain-dependent yield limits (the term “yield limits” is inappropriate since what is limited are only the stresses, while the “boundaries” apply also to strains, as required for softening damage).

Beginning from 1996,¹⁰ a series of progressively improved explicit microplane damage models have been developed for plain and fiber-reinforced concrete, textile composites, shale and other rocks.^{11,12} They have been extensively used as user's material models in the form of explicit Fortran subroutines in, for example, VUMAT of ABAQUS. Based on dynamic relaxation, the explicit FE programs are effective computationally, but sometimes the errors due to artificial inertia and damping may be troublesome. To avoid unstable growth of the numerical dispersion, the time step in an explicit difference scheme must be limited by a certain critical value.¹³ In addition, accurate checks for stability and bifurcation are not obtainable from explicit FE programs.

So far, no method has been available to convert these explicit microplane models with boundaries to a form usable in implicit FE programs. Such a conversion is, however, needed to obtain the acoustic stiffness tensor for detecting localization instabilities, as well as the structural stiffness matrix for assessing structural stability and bifurcation. In addition, the conversion will enhance the applicability of microplane theory into more general frameworks, for example, mesh-free¹⁴ and phase-field modeling.¹⁵ The method to make such a conversion is presented here.

One reason why theoreticians in computational mechanics favored the implicit microplane models was that these models are easily obtained from a potential guaranteeing thermodynamic restrictions.^{16,17} However, the resulting material model was primitive, with a rather limited data fitting capability. Often only a few qualitative response curves, with no data comparisons, were presented as examples [16, e.g.]. No boundary inequalities and no history variables were considered. Analytically defined potential-based total stress-strain curves were used on the microplane, and it was trivial to convert them to a tangent rate form, simply by taking the derivatives of these curves.

In 2011, however, it was shown that formulations based on thermodynamic potentials are not limited to simplistic microplane models with no ability to represent real materials. It was demonstrated that a microplane model with boundary inequalities, such as M7, can also be based on thermodynamic potentials and guarantee the dissipation inequality.^{18,19} To this end, it became necessary to introduce a combination of several separate thermodynamic potentials, governing the elastic behavior, tensile damage, and shear-compression damage with frictional slip, including the inequalities coupling and decoupling them (see the appendix of Caner et al.¹⁹). In addition, the separate treatment of frictional slip eliminated the need for the so-called nonassociated models (typically used for soils) while guaranteeing nonnegative energy dissipation.

However, in contrast to the simple initial thermodynamics-based microplane models,^{16,17} a tangent rate form of the microplane stress-strain relation with boundaries did not ensue. Conversion to a form usable in implicit programs is not guaranteed by using thermodynamic potentials and needs to be done differently, as demonstrated here for microplane model M7.

2 | GENERAL OVERVIEW OF MICROPLANE MODEL

All microplane models stem from Taylor's²⁰ idea of representing inelastic behavior of materials by relations between the stress and strain vectors on planes of various orientations in the microstructure, initially called slip planes and later named microplanes, to also cover fracturing. Initially, the microplanes were considered to be under static constraint, i.e., the microplane stress vector was considered to be a projection of the stress tensor.²¹ This works well for hardening plasticity and is still used in the so-called Taylor models for polycrystalline metals.²²⁻³¹

In the 1980s,^{2,32} it was found that, to ensure stability of the microplane system for strain-softening quasibrittle materials undergoing distributed damage, one must consider the kinematic constraint, in which the microplane strain vectors are the projections of the strain tensor. Such a constraint lends itself easily to an explicit algorithm. The material constitutive law calculates the microplane stress vector from the microplane strain vector on a generic microplane of any spatial orientation within the microstructure. The continuum stress tensor is then computed variationally, from the principle of virtual work which integrates the work of the stress vectors on microplanes of all spatial orientations and equates it to the virtual work of the stress tensor. In computation, integration over all of the spatial orientations is replaced by a summation over a discrete system of microplanes based on an optimal Gaussian formula for integration over a spherical surface.^{33,34} Minimally, 21 microplanes per hemisphere are needed, but typically 37 are used in M7 for better accuracy. In total, M7 is equivalent to 111 (3×37) simultaneous loading surfaces.

The microplane model is a kind of softening multisurface plasticity in which one loading potential with a tensorial form is implied on each microplane. Multisurface plasticity, proposed by Koiter³⁵ and rigorously formulated by Simo et al.,³⁶ was shown by Phillips^{37,38} and Ashby³⁹ to represent the physical reality. But in tensorial form it proved prohibitively difficult to use in computations.

Thanks to its multisurface nature, the microplane approach has five advantages over the classical tensorial models of inelastic behavior:

- (1) Vertex effect, which, in the language of plasticity, is imagined as a vertex ever present at the current state point on the loading surface in the 9D stress space. It means that the response to a stress increment parallel to the current loading surface in the stress space is inelastic rather than elastic, as if the loading surface had a vertex (or corner) at every state point. Consequently, the incremental stiffness for a loading increment oriented parallel to the current loading surface is lower than the elastic stiffness. Such behavior has been implied by Koiter's multisurface plasticity³⁵ and has been demonstrated experimentally for concrete. For example, in the case of torsion superposed on inelastic compression of a cylinder, the classical plasticity models predict elastic torsional stiffness, but experiments showed that, for concrete cylinders under postpeak uniaxial compression, the torsional stiffness can get reduced below 1/4 of the elastic value.⁴⁰ This is predicted correctly by the microplane models, thanks to simultaneous activation of loading surfaces on microplanes of various orientations, but the tensorial damage-plastic models with just a few loading potentials, based on invariants, cannot capture it. The vertex effect is important for dynamic behavior—for example, seismic loads or impact, which often superpose shear on previous inelastic compression—but it has been systematically ignored in computational mechanics.
- (2) Internal friction is not merely a relation between J_2 and I_1 . In reality, the frictional slip occurs only on some planes of specific orientations. This is automatically captured by the microplanes but not by tensorial models based on invariants such as Mohr–Coulomb or Drucker–Prager.
- (3) There is no need for nonassociated plasticity to describe dilatant frictional slip. Thanks to interactions among microplanes, M7 automatically exhibits nonassociated dilatancy observed in concrete, and does so without violating the dissipation inequality of thermodynamics.
- (4) In the vectorial forms, it is easy to take into account the strain dependence of the boundary limits, while for the yield limits in the tensorial formulation with invariants it would be difficult.
- (5) The microplane model automatically predicts the effect of crack-parallel stress on the Mode I fracture energy, G_f , which was recently demonstrated by a new kind of experiment—the “gap test.”^{41,42} Under high crack-parallel compression, G_f of concrete can get doubled or reduced to almost zero. This phenomenon is caused by frictional dilatant slip on microcracks inclined to the crack direction and splitting bands ahead of the crack tip. However, this phenomenon cannot be represented by zero-width line crack models, such as the cohesive crack model (CCM)^{43–45} or the extended finite element model (XFEM),⁴⁶ and also not by the existing tensorial damage models based on invariants.

3 | BASIC MICROPLANE EQUATIONS

The microplane theory defines a constitutive relation between the stress and strain components on a generic plane of any orientation in the microstructure (hence the name microplane). The normal and tangential strains and stresses on a microplane of unit normal n_i (Figure 1) can be defined as:

$$\epsilon_N = N_{ij}\epsilon_{ij}, \quad \epsilon_L = L_{ij}\epsilon_{ij}, \quad \epsilon_M = M_{ij}\epsilon_{ij}, \quad (1)$$

$$\sigma_N = \sigma_N(\epsilon_N, \epsilon_L, \epsilon_M), \quad \sigma_L = \sigma_L(\epsilon_N, \epsilon_L, \epsilon_M), \quad \sigma_M = \sigma_M(\epsilon_N, \epsilon_L, \epsilon_M). \quad (2)$$

According to the kinematic constraint of the microplane model, the normal and shear projections of the strain tensor increment $\Delta\epsilon_{ij} = \epsilon_{ij} - \epsilon_{ij}^0$ onto a microplane with unit normal n_i , and in-plane coordinate axes l_i and m_i labeled by subscripts L and M , are

$$\Delta\epsilon_N = N_{ij}\Delta\epsilon_{ij}, \quad \Delta\epsilon_L = L_{ij}\Delta\epsilon_{ij}, \quad \Delta\epsilon_M = M_{ij}\Delta\epsilon_{ij}, \quad (3)$$

$$\text{where } N_{ij} = n_i n_j, \quad L_{ij} = (l_i n_j + l_j n_i)/2, \quad M_{ij} = (m_i n_j + m_j n_i)/2. \quad (4)$$

At each integration point of FEs, the 12-step explicit algorithm of model M7, described by eqs. (11)–(32) in Reference 40, begins, in each loading step, with the previous values of microplane variables $\epsilon_V^0, \epsilon_N^0, \epsilon_L^0, \epsilon_M^0$, the initial guess of strain increments $\Delta\epsilon_V, \Delta\epsilon_N, \Delta\epsilon_L, \Delta\epsilon_M$, and current history parameters $\epsilon_N^{0+}, \epsilon_N^{0-}$ (the extreme values reached up to the beginning of the current loading step). The algorithm of the vectorial constitutive model defined on a microplane delivers the values of $\sigma_V, \sigma_N, \sigma_L, \sigma_M$ and history parameters $\epsilon_N^+, \epsilon_N^-$ at the end of the loading step.

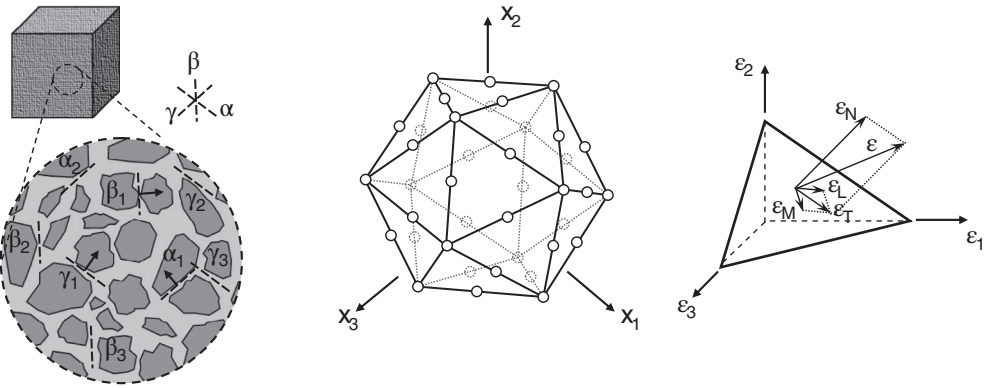


FIGURE 1 *Left:* The planes of inelastic deformations in a representative volume element of particulate composite are imagined to be lumped into one continuum point. *Center:* The normals to radial rays through the circled points on this icosahedron define the system of microplanes. *Right:* Decomposition of strain vector into its normal and shear components along basis vectors ($\mathbf{n}, \mathbf{l}, \mathbf{m}$)

In the M7 algorithm, the stress tensor at the end of the loading step is then obtained from eq. (6) of Caner and Bažant,⁴⁰

$$\sigma_{ij} = \frac{3}{2\pi} \int_{\Omega} (N_{ij}\sigma_N + L_{ij}\sigma_L + M_{ij}\sigma_M) d\Omega \quad (5)$$

which is based on a variational virtual work equation (Ω = surface of a unit hemisphere).

4 | EXPLICIT-IMPLICIT CONVERSION ON MICROPLANE COMPONENT LEVEL

The increments of microplane stresses are

$$\Delta\sigma_N = \sigma_N - \sigma_N^0, \quad \Delta\sigma_L = \sigma_L - \sigma_L^0, \quad \Delta\sigma_M = \sigma_M - \sigma_M^0. \quad (6)$$

The convergence robustness of the incremental-iterative implicit algorithms gets optimized by starting the Newton–Raphson iterations with the elastic stiffness. Specifically, we use the elastic stiffnesses in relating microplane strain increments to the inelastic stress increments $\Delta\sigma_N'', \Delta\sigma_L'', \Delta\sigma_M''$ in the predicting step:

$$\Delta\sigma_N = E_N \Delta\epsilon_N - \Delta\sigma_N'', \quad \Delta\sigma_L = E_T \Delta\epsilon_L - \Delta\sigma_L'', \quad \Delta\sigma_M = E_T \Delta\epsilon_M - \Delta\sigma_M''. \quad (7)$$

These equations are analogous to eq. 6 of Bažant and Prat⁴. Note that, E_N and E_T are the linearized normal and tangent stiffnesses at each loading increment. Since they depend on the stress and strain of the previous loading increment and on the history variables, they are considered constant in the loading step iterations. However, if the predicted stress exceeds the stress boundary, it gets corrected. This correction will also affect the consistent tangent moduli tensor, hence guaranteeing the convergence.

Comparisons with Equation (6) yield the inelastic microplane stress increments (or eigenstrains):

$$\Delta\sigma_N'' = E_N \Delta\epsilon_N - (\sigma_N - \sigma_N^0), \quad (8a)$$

$$\Delta\sigma_L'' = E_T \Delta\epsilon_L - (\sigma_L - \sigma_L^0), \quad (8b)$$

$$\Delta\sigma_M'' = E_T \Delta\epsilon_M - (\sigma_M - \sigma_M^0). \quad (8c)$$

These simple relations are the key step in the conversion.

To reach to the equilibrium state of the current step, the predictor–corrector algorithm shown in the above three equations has been implemented. First, the values of the microplane stresses are estimated based on assuming elastic behavior. If the prediction exceeds the corresponding components on the boundary, a correction is made by a stress drop to the boundary at constant strain (which may be seen as the special case of the algorithm of radial return in the strain space). During this correcting step, the tangent stiffness of each component is also modified. As the inelastic strains and tangent stiffness in each iteration are computed from the currently updated displacement field, the implicit form on the microplane level is attained separately for each component.

5 | MICRO-MACRO TRANSITION TO TENSORIAL INCREMENTAL STRESS-STRAIN RELATION

Now we can proceed similarly to Equation (5) (analogous to eqs. (11–14) of Bažant and Prat⁴), which is based on the variational principle of virtual work and gives the corresponding incremental tensor of inelastic strain:

$$\Delta\sigma_{ij}'' = \frac{3}{2\pi} \int_{\Omega} (N_{ij}\Delta\sigma_N'' + L_{ij}\Delta\sigma_L'' + M_{ij}\Delta\sigma_M'') d\Omega. \quad (9)$$

The incremental constitutive equation of the implicit algorithm for an integration point of one FE then reads:

$$\Delta\sigma_{ij} = C_{ijkl}^{el} \Delta\epsilon_{kl} - \Delta\sigma_{ij}'', \quad (10)$$

where C_{ijkl}^{el} is the elastic stiffness tensor, which depends on the previous loading step (based on its converged iteration) but not on the current step (or current iteration). For concrete as an (approximately) isotropic material, this tensor, or the corresponding elastic 6×6 stiffness matrix, is constructed from the elastic constants, either E and ν or K and G , and from the history variables $\epsilon_N^{0+}, \epsilon_N^{0-}$. According to eq. (9) of Caner and Bažant,⁴⁰ $E_{N0} = E/(1-2\nu)$ is the pristine microplane normal elastic stiffness and $E_T = E_{N0}(1-4\nu)/(1+\nu)$ is the pristine microplane elastic shear stiffness (tangent to microplane), which is the same for the orthogonal L and M directions of the shear components on the microplane.

The incremental stress–strain relation in Equation (10) is then used, in matrix form, in step-by-step structural analysis, normally with iterations in each increment.

6 | CONSISTENT TANGENT MODULUS

The variational equation based on the principle of virtual work may be written as:

$$\delta\sigma_{ij} = C_{ijkl}^t \delta\epsilon_{kl} = \frac{3}{2\pi} \int_{\Omega} (N_{ij}\delta\sigma_N + L_{ij}\delta\sigma_L + M_{ij}\delta\sigma_M) d\Omega. \quad (11)$$

Here, we may introduce tangent stress–strain relations $\delta\sigma_N = E_{NN}^t \delta\epsilon_N + E_{NL}^t \delta\epsilon_L + E_{NM}^t \delta\epsilon_M$, which gives

$$\delta\sigma_N = E_{NN}^t N_{kl} \delta\epsilon_{kl} + E_{NL}^t L_{kl} \delta\epsilon_{kl} + E_{NM}^t M_{kl} \delta\epsilon_{kl}, \quad (12)$$

$$\delta\sigma_L = E_{LN}^t N_{kl} \delta\epsilon_{kl} + E_{LL}^t L_{kl} \delta\epsilon_{kl} + E_{LM}^t M_{kl} \delta\epsilon_{kl}, \quad (13)$$

$$\delta\sigma_M = E_{MN}^t N_{kl} \delta\epsilon_{kl} + E_{ML}^t L_{kl} \delta\epsilon_{kl} + E_{MM}^t M_{kl} \delta\epsilon_{kl}. \quad (14)$$

This yields an equation where $\delta\epsilon_{kl}$ can be factored out of all the terms. For this equation to be valid for any $\delta\epsilon_{kl}$, the expression that is multiplied by $\delta\epsilon_{kl}$ must vanish. This result is:

$$C_{ijkl}^t = \frac{3}{2\pi} \int_{\Omega} \left(N_{ij}N_{kl}E_{NN}^t + N_{ij}L_{kl}E_{NL}^t + N_{ij}M_{kl}E_{NM}^t \right. \quad (15a)$$

$$\left. + L_{ij}N_{kl}E_{LN}^t + L_{ij}L_{kl}E_{LL}^t + L_{ij}M_{kl}E_{LM}^t + M_{ij}N_{kl}E_{MN}^t + M_{ij}L_{kl}E_{ML}^t + M_{ij}M_{kl}E_{MM}^t \right) d\Omega. \quad (15b)$$

This is the consistent tangent moduli tensor, which is in general nonsymmetric (nonetheless, the energy dissipation is ensured to be nonnegative⁴⁰). Based on how the microplane stresses have been formulated, $E_{NM} = E_{NL} = 0$, that is, the normal stress on a microplane is independent of the shear strain on the same surface. But the opposite is not true, that is, $E_{MN}, E_{LN} \neq 0$. Also note that this computation implies the stresses on each microplane not to depend on the stresses and strains on other microplanes.

7 | ADJUSTMENT TO M7 ALGORITHM NEEDED FOR IMPLICIT VERSION

The algorithm of explicit M7 was defined by eqs. (11)–(32) in Reference 40. One step, however, implies a small discontinuous jump in the shear stress at the boundary σ_b^τ , which prevents convergence of Newton–Raphson type iterations in an implicit algorithm. Rather it causes back-and-forth switching between the equations for positive σ_N and for negative σ_N (which implies, through eq. (26) of Caner and Bažant,⁴⁰ different values of ϵ_V and thus leads to back-and-forth switching of the Jacobian).

The jump is here replaced by a smooth transition. To this end, eqs. (27) and (28) from Caner and Bažant⁴⁰ are now replaced by one equation:

$$\sigma_b^\tau = \frac{1}{2} [1 - \tanh(\sigma_N/s')] R_{27}(\sigma_N, \epsilon_V) + \frac{1}{2} [1 + \tanh(\sigma_N/s)] R_{28}(\sigma_N, \epsilon_V), \quad s = 0.1Ek_1, \quad (16)$$

where parameter s , introduced empirically, governs the width of the transition range; $R_{27}(\sigma_N, \epsilon_V)$ and $R_{28}(\sigma_N, \epsilon_V)$ are the right-hand sides of eqs. (27) and (28) from Caner and Bažant,⁴⁰ with ϵ_V introduced through eq. (26). Note that, for $s \rightarrow 0$, tanh would converge to the Heaviside step function, which would make Equation (16) equivalent to eqs. (27) and (28) of the original M7 algorithm in Reference 40. Therefore, while s should be chosen as small as possible, it must not be chosen too small.

This correction also improves the original explicit algorithm of M7. Particularly, it improves its convergence when the loading step is decreased to zero.

What facilitated our explicit–implicit conversion is that it could be made on the microplane level where we deal with components of scalar stress–strain relations rather than tensor components bound by tensorial transformation rules. Doing the same between the tensorial stress and strain components on the macro-level would be wrong, as it would violate the conditions of tensorial invariance. This is actually another advantage of the microplane approach to the constitutive modeling of damage.

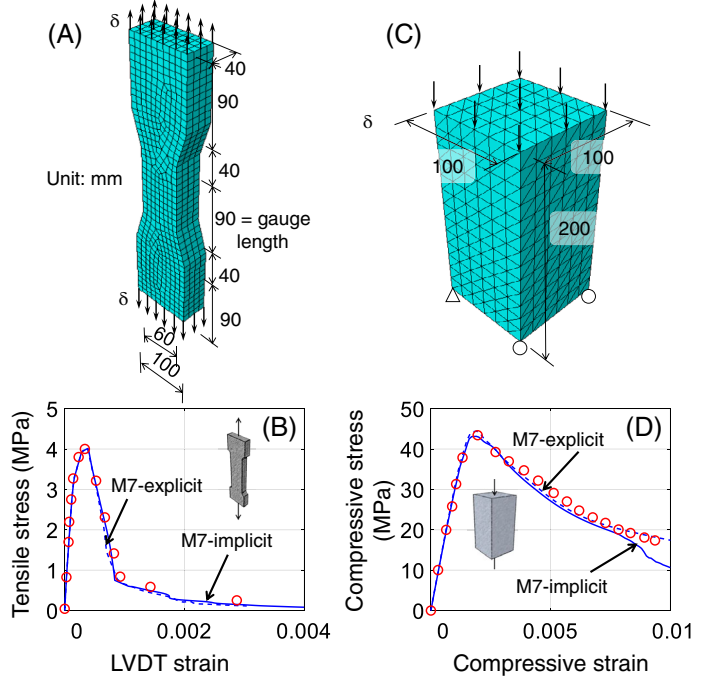
The crucial point has been to make the conversion at the end of the microplane constitutive algorithm—that is, neither within this algorithm nor later on the tensorial level—and then transform the incremental scalar form on the microplanes into a tensorial one on the continuum macro-level.

Although the M7 version of microplane model is selected in this study, thanks to its success in representing all kinds of material test data for concrete, similar explicit–implicit conversions can be made in other microplane models with boundary inequalities. A few examples can be listed, such as the anisotropic spherocylindrical microplane model¹¹ for shale, the triad-microplane model^{12,47} for textile twill composites, or the fatigue microplane model for concrete.⁴⁸

8 | SEVEN EXAMPLES OF EXPLICIT-IMPLICIT-EXPERIMENTAL COMPARISONS FOR MICROPLANE MODEL M7

The accuracy of the implicit algorithm for M7 is now validated by simulating seven characteristic experiments, comparing the implicit results to explicit, and also by demonstrating that the test data are represented by M7 realistically. In numerical integration over the hemisphere, 37 integration points are used, in which case the optimal Gaussian integration formula

FIGURE 2 Comparison of M7-implicit with M7-explicit, and experimental data for concrete prisms under: (A, B) direct tension, and (C, D) uniaxial compression



is capable of integrating exactly polynomials up to the 13th degree. Tetrahedral or hexahedral elements were generated with a “free-mesh” algorithm embedded in ABAQUS, to suppress the orientation biases.

To eliminate the spurious mesh sensitivity, computer simulations were made with the crack-band model, in which the FE sizes in the fracture area are decided on the basis of the fracture process zone size. This size, in turn, is approximately proportional to the maximum size of the material heterogeneity, here the maximum aggregate size, although the relative stiffnesses and strengths of mortar, aggregate and interface zone also matter.

8.1 | Postpeak softening damage under uniaxial tension

Figure 2(B) demonstrates close agreement of the results obtained by the implicit and explicit algorithms on a uniaxial tensile experiment. Both also fit closely the results of the tests reported in Reference 49. In this test, the dog-bone specimens, whose dimensions were $100 \times 350 \times 40$ mm, were subjected to uniaxial tensile load (see Figure 2(A)). Neither the load nor displacement control could produce stable postpeak softening response, so a linear variable differential transformer (LVDT) was mounted at the middle segment of specimen, to control the test. The gauge length was 120 mm, spanning a section with FE size of 9 mm. The M7 calibrated parameters were $k_1 = 0.00011$, $k_2 = 100$, $k_3 = 20$, $k_4 = 40$, $E = 28,600$ MPa. The boundary condition and the meshed domain are also shown in Figure 2(A).

The small deviations of explicit from implicit, seen in Figure 2(B), must be attributed to the propagation of a numerical wave generated by error accumulation. Note that, due to the nonsymmetry of the Jacobian, the global stiffness matrix must be stored in ABAQUS with the nonsymmetric option, or else it would be challenging to get the simulations to converge.

8.2 | Postpeak softening damage under uniaxial compression

Figure 2(D) demonstrates a good explicit–implicit agreement, as well as a close fit of the uniaxial compressive test data by van Mier.⁵⁰ Concrete prisms with dimensions $100 \times 100 \times 200$ mm were subjected to monotonically increasing compressive stress. The FE size was 16 mm. As seen in Figure 2(D), the implicit result diverges from the explicit result only for very large strain, by >8%, which is due to a difference in the localization pattern. In this simulation, the experimentally calibrated M7 parameters were $k_1 = 0.000142$, $k_2 = 110$, $k_3 = 12$, $k_4 = 38$, $E = 33,500$ MPa. See Figure 2(C) for the imposed boundary conditions and the mesh.

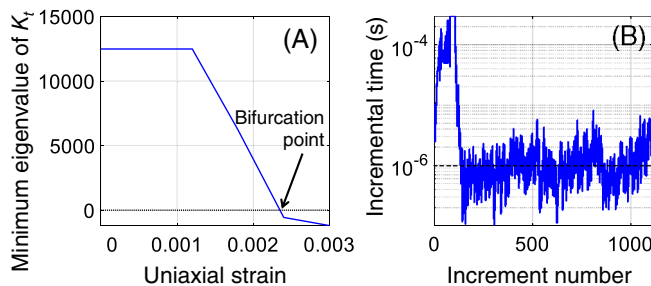


FIGURE 3 (A) The gradual decrease of the minimum eigenvalue of the global stiffness matrix; and (B) the evolution of the increment time during the loading process

In both direct tension and uniaxial compression, the question of strain localization and mesh sensitivity arises. In a homogeneous medium, the ellipticity of the problem will weaken when one or more elements experience softening. However, such a reduction will pose a challenge to the equation solver due to an abrupt change in the global stiffness matrix. Therefore, a 1% random perturbation of k_1 (eqs. (11–32) in Reference 40) was generated in the implicit simulation to prevent multiple elements entering softening regime at the same iteration. In the explicit version, this was taken care of by random numerical dispersion generated over time by the cumulative error. Physically, this reflects the role of random flaws in the real specimens.

One valuable feature of the explicit–implicit conversion is that the implicit scheme allows querying the global stiffness matrix. On the structural scale, accumulation of microcracks can weaken the ellipticity of the boundary value problem.⁵¹ Once the ellipticity of a partial differential equation is lost, either instability or bifurcation will arise (as, e.g., at a limit point of the load-deflection curve). This can be quantified by checking the eigenvalues of the tangent stiffness matrix of the structure. After the limit point, the load increment should follow a more stable path. In the case there exists more than one stable paths, the path that maximizes entropy of the system (or minimizes the Helmholtz free energy, or the second-order work) will automatically occur [51, p651].

The minimum eigenvalue of the total tangent structural stiffness matrix \mathbf{K} is calculated to detect the loss of uniqueness or stability, which indicates the onset of strain localization. After that, the boundaries on microplane of all different orientations, 111 (3×37) in number, lead, along with the present introduction of a smooth transition function (16)), to a gradual development of damage at the material points. This is manifested in the gradual decrease of the lowest eigenvalue λ_1 of \mathbf{K} , shown in Figure 3(A), as the damage accumulates at microplanes of various orientations at various integration points of FEs. When the first eigenvalue vanishes, a discontinuity in the displacement field appears. The eigenvalues were computed by inserting eigenvalue analysis steps in each loading step, which yields a piece-wise approximation to eigenvalue evolution.

Similar to other strain-softening constitutive laws, the time step had to be reduced, so as to improve the convergence of the iterations within the step (Figure 3(B)). However, this step reduction stabilized at a certain level, which proves the implicit algorithm to be stable even at a large strain, that is, when further damage arises (this feature has been unavailable in some tensorial damage models with unrealistic softening behavior, which has caused the time step to vanish at large strain).

The convergence rate of the implicit algorithm is documented in Figure 4. The four data points separate four stages on the uniaxial load-displacement curve: weakly nonlinear prepeak state (with only sparse microcracks), onset of postpeak softening, steep postpeak softening (dense cracks begin to coalesce into a band), and a fully softened state (a macrocrack appears and widens). This figure shows that the decrease of the norm of the residual relative displacement $y_{n+1} - y_{n+1}^k$ with the iteration number k . Convergent iterations follow a power law

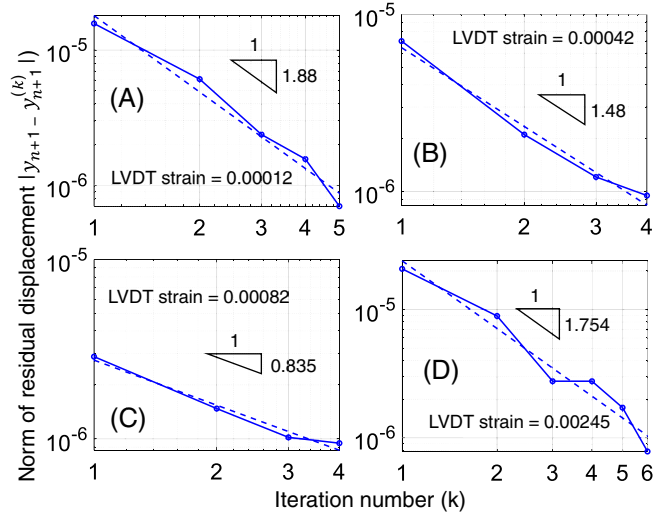
$$y_{n+1} - y_{n+1}^k = C k^{-p}, \quad (17)$$

where C and p are constants. Exponent $p = 2$ represents quadratic convergence, characterizing elastic structures. Since y_{n+1} is the converged solution at step $n + 1$, we take logarithms of this equation and use a nonlinear optimization algorithm such as Levenberg–Marquardt (e.g., in MatLab), to minimize

$$[\log(y_{n+1} - y_{n+1}^k) + p \log k - C]^2 \rightarrow \min. \quad (18)$$

This yields the values of p , C providing the optimum least-square fit of iterates $y_{n+1} - y_{n+1}^k$ by Equation (17), and allows plotting the convergence diagrams in Figure 4. Cases (A) and (D), which correspond to a prepeak nonlinear state and a

FIGURE 4 Convergence analysis showing the decrease of residual displacement (or error), indicated by the linear variable differential transformer (LVDT) strain, with the number of iterations, plotted in log-log scale. Cases (A) and (D), corresponding to elastic prepeak and fully softened crack band, are close to quadratic convergence (slope 2), while in the postpeak state with steep softening the convergence is slower (slope <1) yet does occur



state with a fully softened crack band, give an almost quadratic convergence. In cases (B) and (C), corresponding to the peak state and to the steep softening with localization into a band under way, the convergence is slower, but does take place.

8.3 | Vertex effect in tests of torsion superposed on compression

The vertex effect, mentioned earlier, is the most important difference from the classical tensorial models based on loading potentials in the stress space. A very strong vertex effect in superposing a small shear stress increment upon a large uniaxial compression was demonstrated by the compression-torsion experiments of Caner et al.,⁵² conducted on cylindrical specimens of concrete with dimensions 101.6×203.2 mm. Using an MTS axial-torsional testing machine, a uniaxial compression reaching into various stages of postpeak was applied and then followed by a torsional rotation. A major vertex effect was demonstrated by these tests. It is important, for example, for the seismic loading of buildings, in which large shear strains are suddenly superposed on axial compression.

Simulations again demonstrated an excellent implicit-explicit agreement, and also agreed satisfactorily with the test results; see Figure 5(A,B). The maximum principal strain fields corresponding to three corresponding uniaxial strains in Figure 5(B) were presented in 5(C). The element size was, in this case, 9 mm and the calibrated M7 parameters were $k_1 = 0.00013$, $k_2 = 90$, $k_3 = 30$, $k_4 = 70$, $E = 36,900$ MPa. Figure 5(C) also shows the loading apparatus and the mesh size of this simulation.

The standard tensorial constitutive laws based on stress or strain invariants and potential surfaces in the stress space cannot simulate the vertex effect. In Figure 5(B) they give a horizontal line, as marked. In 1960s and 1970s the vertex effect caused excitement in the continuum mechanics community and was extensively debated, but with no successful solution.^{21,37,38,53-60}

8.4 | Postpeak behavior under cyclic and mixed-mode loading

Another capability of the implicit version is to capture, as closely as the explicit version, the hysteresis of loading-unloading cycles in concrete, with realistic loops (see Figure 6(A,B)). This is enabled by the predictor-corrector process in each microplane. In Figure 6, the experimental data by Sinha et al.⁶¹ were obtained from cyclic uniaxial compressive tests on concrete cylinders with $D = 76.2$ mm and $h = 152.4$ mm. The cylindrical specimens were subjected to several cycles of loading and unloading under displacement control. The fitting results using the present model (with parameters $k_1 = 0.000103$, $k_2 = 70$, $k_3 = 20$, $k_4 = 70$, $E = 21,374$ MPa and FE sizes of 9 mm) showed a good agreement between explicit and implicit algorithms and also with the experiments. The cyclic response followed a load path different from the monotonic uniaxial load which represented the load-displacement envelope. The strength limit decreased and departed from such an envelope, which manifested an essential feature of fatigue. The energy dissipated in each cycle, represented by the area swept by a loading-unloading cycle, reflected a comparable amount of dissipation between

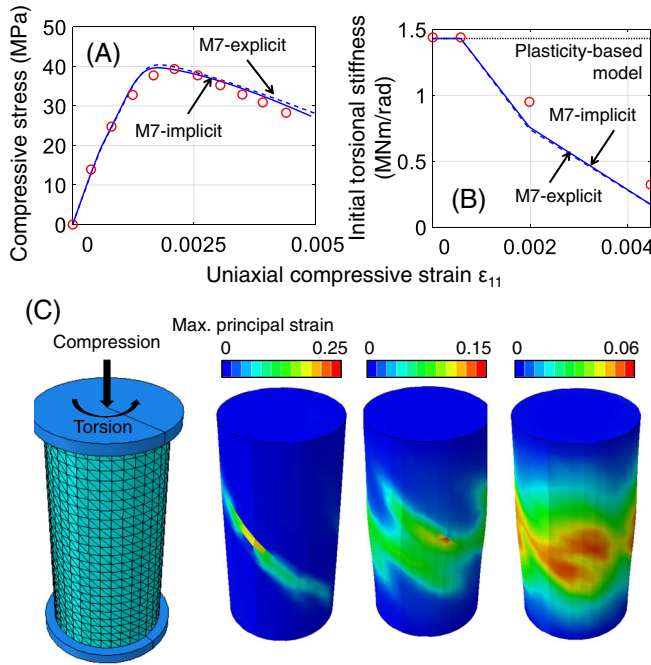


FIGURE 5 (A) The average of uniaxial compression of 4 × 8 in. cylinder; (B) A comparison of the vertex effect between M7-implicit, M7-explicit, and experiments by Caner et al.⁵²; and (C) The strain field after torsion corresponding to different applied uniaxial strain

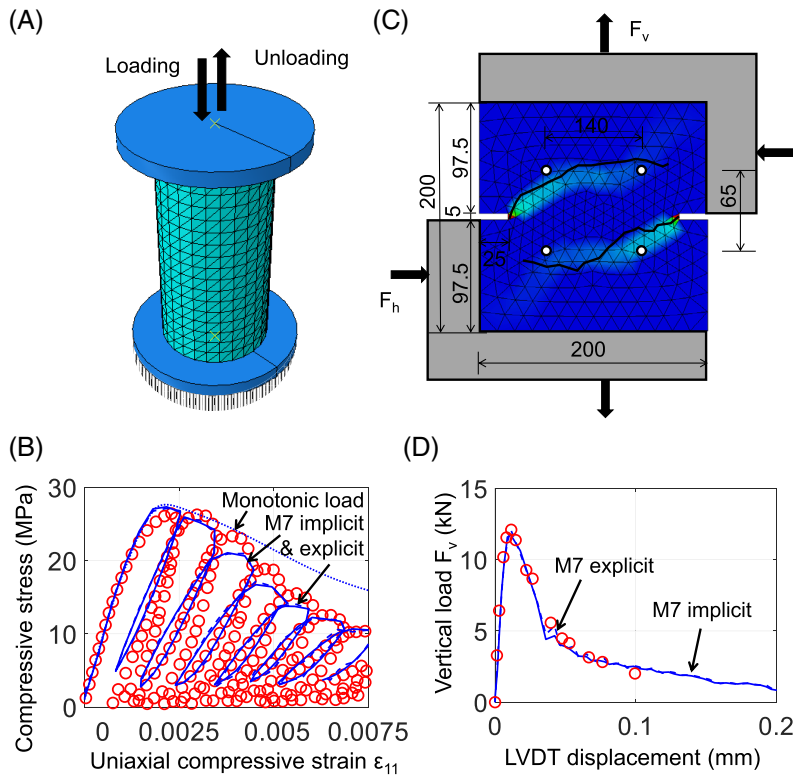


FIGURE 6 F(A) Comparison of M7-implicit with experiments: (A, B) cyclic uniaxial compressive test, and (C, D) tension-shear test with $F_h = 10$ kN

simulations and experiments. These suggested a good characterization of opening and closing microcracks represented by various microplanes.

8.5 | Fracture of double-edge-notched specimen

As another example, we choose the four-point loading of the double-edge-notched specimen. The loading is often labeled “mixed-mode” even though, in concrete, the cracks propagate in Mode I despite shear force in the ligament. This test checks the ability to capture the direction of crack path.

Nooru-Mohamed⁶² performed several experiments in which the vertical and horizontal loads were applied in different manners. Here, we simulate only one of his tests. The specimen dimensions are shown in Figure 6(C). In the first step, the horizontal load F_h was increased to 10 kN while δ_v was kept constant. In the second step, the vertical tensile displacement δ_v corresponding to vertical load F_v was raised up to failure while F_h ceased to change. F_v was recorded while the displacements were applied. Both the crack path and load-LVDT (whose attachment points are shown in Figure 6(C,D)) in the experiments were well captured by explicit and implicit versions; see Figure 6(C,D)). The parameters used in the simulations are $k_1 = 0.000089$, $k_2 = 60$, $k_3 = 20$, $k_4 = 50$, $E = 30,500$ MPa with elements' sizes of 16 mm, approximating the coarse aggregate size of the utilized concrete.

8.6 | Pure Mode II fracture of 4-point-loaded double-edge-notched specimens

In the case of sliding of a geological fault,⁶³ a crack opening is prevented by enormous hydrostatic pressure. In absence of high hydrostatic pressure, the cracks in concrete prefer to run, as opening Mode I cracks, along the principal stress direction, as manifested in Figure 6(C). However, when the zone of high shear stress is a very narrow strip, a crack that would extend in the principal stress direction would run into this zone of low stress associated with a lower energy release rate. This is one cause of straight-ahead propagation in Mode II. Another, perhaps more important, cause is a high crack-parallel compression, which probably greatly reduces the Mode II fracture energy, as suggested by the gap tests.^{41,42}

Both causes come to play in the double-edge-notched specimen if the opposite loads are placed close to the notches, as in Figure 7(A). The crack will then run straight ahead in pure shear, Mode II, as demonstrated in the 1996's experiments of Bažant and Pfeiffer⁶⁴ (Figure 7). These experiments allowed determining the Mode II fracture energy by the size effect method,⁴⁵ based on the measured peak loads of geometrically similar specimens of 4 sizes (Figure 7(C)), with beam depths $D = 38.1, 76.2, 152.4$, and 304.8 mm. The thickness of all specimens was 38.1 mm (see Figure 7), so as to achieve two-dimensional scaling.

Figure 7(B) shows the curve of the size effect law

$$\sigma_N = \frac{\sigma_0}{\sqrt{1 + D/D_0}} \quad (19)$$

obtained by fitting the nominal strengths, σ_N , to the results of FE simulations with the implicit microparticle model M7. The optimal fit of this curve to the measured data points is seen to be as close as the scatter allows. The asymptote of this curve determines the Mode II fracture energy, G_f^II (the free parameters of M7 were $k_1 = 0.000076$, $k_2 = 40$, $k_3 = 15$, $k_4 = 46$, $E = 28,100$ MPa, and element size was 6 mm for all D). According to the linear regression of size effect

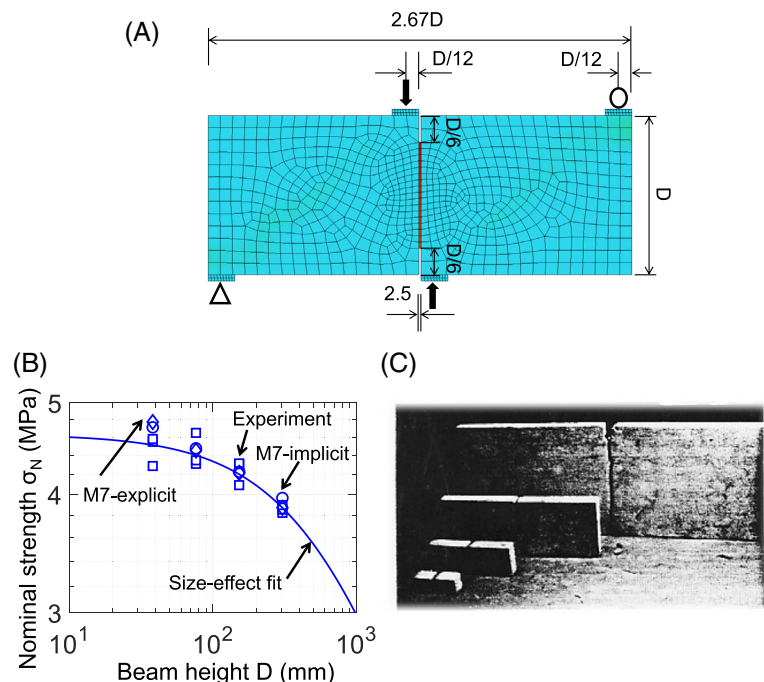


FIGURE 7 Comparison of M7-implicit with experiments of pure Mode II fracture of double-edge-notched specimen: (A) specimens geometry and crack path at peak load documenting pure Mode II crack propagation; (B) peak loads of geometrically similar specimens with $D = 38.1, 76.2, 152.4, 304.8$ mm; and (C) test specimens of Bažant and Pfeiffer⁶⁴ as seen after the tests, with a straight Mode II fracture visible on the largest specimen

method, the critical fracture energy release rate and the material characteristic length are obtained as $G_f^{II} = \sigma_0^2 g_0 D_0$ and $c_f = (g_0/g'_0)D_0$, where $g_0 = g(a_0/D)$ and $g'_0 = g'(a_0/D)$; $g(\alpha)$ is the dimensionless LEFM fracture energy release rate and a function of the relative crack length $\alpha = a/D$ corresponding to the specimen geometry and loading configuration (a = crack length).

The ability of capturing fracture under mixed-mode load and fracture in the last two examples is essential to represent the effect of crack-parallel stress σ_{xx} .^{41,42} This is because the triaxial state of the crack tip is appropriately captured by interaction among the stress components on microplanes. Thanks to this feature, complex phenomena such as friction interlock and dilatant expansion corresponding to different level of parallel stress can be appropriately quantified, which will be discussed next.

8.7 | The effect of stress σ_{xx} parallel to the crack on the failure load revealed by gap tests

In a new type of experiment, called the “gap test,” Nguyen et al.^{41,42} have shown that a compressive stress σ_{xx} parallel to the crack plane has a major effect on the fracture energy, G_f . The test uses notched three-point-bend beams with two simple but crucial modifications—the end supports are installed with gaps and loading pads are added on the sides of the notch. The pads are made from an almost perfectly plastic material. Thus, the initial loading produces at the FPZ an almost constant and uniform crack-parallel stress σ_{xx} . After that, the gaps at the ends close, and further loading produces a bending moment M that opens the crack in presence of a constant crack-parallel compression.

If the FPZ were a point and the crack a line crack, this compression could have no effect on the moment-displacement curve. But it does and, in fact, has a major effect. This effect cannot be captured by line-crack models, including LEFM, XFEM, and CCM.^{46,65,66} A model with a realistic tensorial damage model for an FPZ of finite width is obviously required.

The data points in Figure 8(C), where σ_c is the maximum compressive stress, represent the measured peak loads $F_M = 4M/L$ corresponding to the bending moment; F_M = load in excess of the reaction from the plastic pads, L = span = 381mm, D = 101.6 mm. The curve represents the prediction by crack band model with the explicit and implicit microplane model M7 (whose parameters were $k_1 = 0.000127$, $k_2 = 40$, $k_3 = 20$, $k_4 = 36$, $E = 24,500$ MPa). The match of the test data is seen to be satisfactory at 5 levels of crack-parallel compressive stress σ_{xx} . These results reflect similar trend of the fracture energy G_f with respect to σ_{xx} . In fact, by using the size effect method mentioned in the previous section, one can fit the peak loads of geometrically similar specimens ($D=101.6$, 203.2, and 406.4 mm) to obtain G_f at a given level of σ_{xx}/σ_c . The horizontal dashed line shows the prediction of line crack models, including CCM and XFEM based on LEFM. The microstructural mechanism of the crack-parallel stress effect within the FPZ consists of the effects of σ_{xx} on the static and

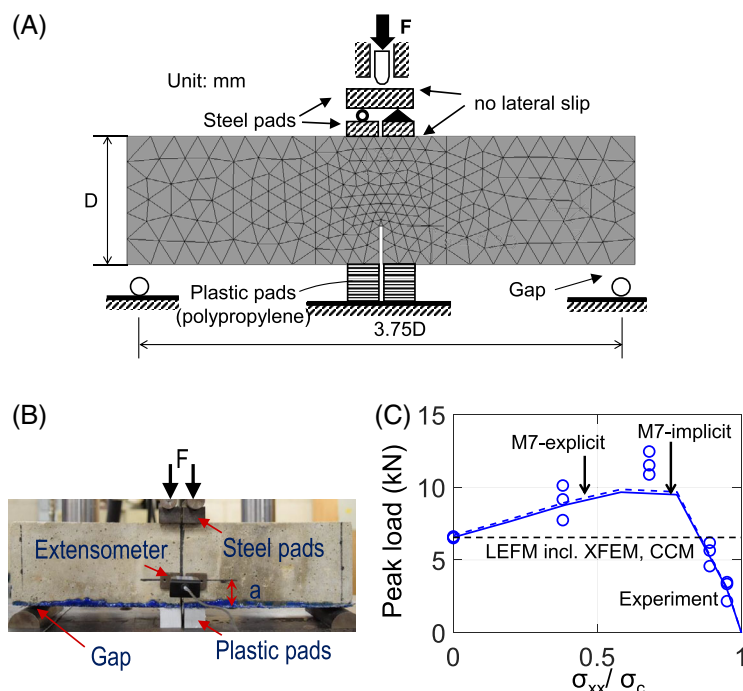


FIGURE 8 (A) Setup of the gap test with $D = 203.2$ mm (8 in.). The size of the elements in the crack front region is 12 mm; (B) Photo of the gap test; (C) Measured peak loads compared with the predictions of the finite element crack band model with implicit microplane model M7, of the LEFM-based extended finite element method (XFEM), and of the cohesive crack model (CCM)

sliding friction on the microcracks inclined to x , on the consequent axial splitting microcracks, and on the change of FPZ width, as explained by Figure 7 in Reference 42.

9 | CONCLUSIONS

1. A microplane model with inequality boundaries can be easily converted from explicit to implicit on the level of the microplane. The entire constitutive algorithm is run on each microplane and then, from the resulting microplane stress, one evaluates, for each microplane, both the inelastic stress increment and the incremental (or tangent) stiffness. The subsequent calculation of the inelastic stress tensor increment or the incremental stiffness tensor is, as usual, based on the variational principle of virtual work, imposing static equivalence of the stress tensor and the microplane stress components.
2. To improve the convergence of loading step iterations with the implicit formulation, a minor adjustment is made by replacing a small volumetric strain jump in the original formulation of M7 by a smooth transition.
3. Seven diverse examples of implicit FE simulations are presented. To show that they are not contrived but realistic, the proposed method can capture the critical features in these experiments that are challenging to fit. The implicit and explicit versions of microplane model M7 are shown to yield virtually identical results, and also to agree with the actual experimental results.
4. The third example at the same time documents the importance of the vertex effect. The microplane model succeeds in vertex modeling because it is essentially equivalent to multisurface plasticity—for the case of microplane model M7 involving over a hundred simultaneous loading surfaces in the vectorial sense.
5. The fourth example showcases the ability to capture the fracture growth under cyclic loading, and gives a good prediction of the energy dissipated in loading–unloading reversal or in an unloading–reloading loop. The fifth and sixth example show that M7 can fit the Mode I fracture under “mixed-mode” loading, as well as the pure shear fracture of Mode II. The seventh example documents a good prediction of the effect of crack-parallel compression on the stress-displacement response measured in the recently developed “gap test,” which is shown to lead to a dependence of fracture energy on crack-parallel stress.
6. There are now over a hundred different constitutive models of concrete in the computational literature, typically shown to fit only about one to three basic type of experiments but none able to fit, for example, the experiments in examples 4 and 7 or most of those used in the calibration of model M7. Although the importance of experimental verification of computational models has long been emphasized, little such effort has been seen.

Note: The coding of the material subroutine of implicit microplane model M7, directly usable in UMAT of ABAQUS, can be freely downloaded from the following website: <http://www.civil.northwestern.edu/people/bazant>.

ACKNOWLEDGMENT

Financial support under NSF Grant CMMI-202964 to Northwestern University is gratefully acknowledged.

ORCID

Zdeněk P. Bažant  <https://orcid.org/0000-0003-0319-1300>

REFERENCES

1. Bažant ZP, Oh BH. Crack band theory for fracture of concrete. *Mater Constr.* 1983;16(3):155-177.
2. Bažant ZP, Oh BH. Microplane model for progressive fracture of concrete and rock. *J Eng Mech.* 1985;111(4):559-582.
3. Bažant ZP, Prat PC. Creep of anisotropic clay: new microplane model. *J Eng Mech.* 1987;113(7):1050-1064.
4. Bažant ZP, Prat PC. Microplane model for brittle-plastic material: I theory. *J Eng Mech.* 1988;114(10):1672-1688.
5. Bažant ZP, Ožbolt J. Nonlocal microplane model for fracture, damage and size effect in structures. *J Eng Mech.* 1990;116(11):2485-2505.
6. Bažant ZP, Ožbolt J. Compression failure of quasibrittle material: nonlocal microplane model. *J Eng Mech.* 1992;118(3):540-556.
7. Ožbolt J, Bažant ZP. Microplane model for cyclic triaxial behavior of concrete. *J Eng Mech.* 1992;118(7):1365-1386.
8. Bažant ZP, Caner FC, Carol I, Adley MD, Akers SA. Microplane model M4 for concrete. I: formulation with work-conjugate deviatoric stress. *J Eng Mech.* 2000;126(9):944-953.
9. Caner FC, Bažant ZP. Microplane model M4 for concrete. II: algorithm and calibration. *J Eng Mech.* 2000;126(9):954-961.
10. Bažant ZP, Xiang Y, Prat PC. Microplane model for concrete. I: stress-strain boundaries and finite strain. *J Eng Mech.* 1996;122(3):245-254.
11. Li C, Caner FC, Chau VT, Bažant ZP. Spherocylindrical microplane constitutive model for shale and other anisotropic rocks. *J Mech Phys Solids.* 2017;103:155-178.

12. Kirane K, Salviato M, Bažant ZP. Microplane-triad model for elastic and fracturing behavior of woven composites. *J Appl Mech.* 2016;83(4):041006-1-041006-14.
13. Courant R, Friedrichs K, Lewy H. On the partial difference equations of mathematical physics. *IBM J Res Dev.* 1967;11(2):215-234.
14. Huerta A, Belytschko T, Fernández-Méndez S, Rabczuk T, Zhuang X, Arroyo M. Meshfree methods. *Encyclopedia of Computational Mechanics.* 2nd ed. Hoboken, NJ: John Wiley & Sons, Inc.; 2018:1-38.
15. Wu J-Y, Nguyen VP, Nguyen CT, Sutula D, Bordas S, Sinaie S. Phase field modeling of fracture. *Advances in Applied Mechanics: Multi-scale Theory and Computation.* Vol 52. Cambridge, MA: Academic Press; 2018.
16. Kuhl E, Ramm E. On the linearization of the microplane model. *Mech Cohesive-frictional Mater Int J Exper Modell Comput Mater Struct.* 1998;3(4):343-364.
17. Carol I, Jirásek M, Bažant Z. A thermodynamically consistent approach to microplane theory. Part I. free energy and consistent microplane stresses. *Int J Solids Struct.* 2001;38(17):2921-2931.
18. Bažant ZP, Wu JY, Caner FC, Cusatis G. How to enforce non-negative energy dissipation in microplane and other constitutive models of softening damage, plasticity and friction. Paper presented at: Proceedings of the Computational Modeling of Concrete structures, EURO-C Conference Schladming/Rohrmoos; 2010:87-91; Taylor & Francis, London, Austria.
19. Caner FC, Bažant ZP, Hoover CG, Waas AM, Shahwan KW. Microplane model for fracturing damage of triaxially braided fiber-polymer composites. *J Eng Mater Technol.* 2011;133(2):021024-1-021024-12.
20. Taylor GI. Plastic strain in metals. *J Inst Met.* 1938;63:307-324.
21. Batdorf SB, Budiansky B. A mathematical theory of plasticity based on the concept of slip. United States. National Advisory Committee for Aeronautics. Washington, DC: National Advisory Committee for Aeronautics; 1949.
22. Kröner E. Zur plastischen Verformung des Vierkristalls. *Acta Metall.* 1961;9(2):155-161.
23. Lin T, Ito M. Theoretical plastic distortion of a polycrystalline aggregate under combined and reversed stresses. *J Mech Phys Solids.* 1965;13(2):103-115.
24. Hill R. Continuum micro-mechanics of elastoplastic polycrystals. *J Mech Phys Solids.* 1965;13(2):89-101.
25. Hill R. Generalized constitutive relations for incremental deformation of metal crystals by multislip. *J Mech Phys Solids.* 1966;14(2):95-102.
26. Rice JR. Inelastic constitutive relations for solids: an internal-variable theory and its application to metal plasticity. *J Mech Phys Solids.* 1971;19(6):433-455.
27. Hill R, Rice J. Constitutive analysis of elastic-plastic crystals at arbitrary strain. *J Mech Phys Solids.* 1972;20(6):401-413.
28. Asaro RJ, Rice J. Strain localization in ductile single crystals. *J Mech Phys Solids.* 1977;25(5):309-338.
29. Pande GN, Sharma K. Multi-laminate model of clays a numerical evaluation of the influence of rotation of the principal stress axes. *Int J Numer Anal Methods Geomech.* 1983;7(4):397-418.
30. Diard O, Leclercq S, Rousselier G, Cailletaud G. Evaluation of finite element based analysis of 3d multicrystalline aggregates plasticity: application to crystal plasticity model identification and the study of stress and strain fields near grain boundaries. *Int J Plast.* 2005;21(4):691-722.
31. Roters F, Eisenlohr P, Bieler TR, Raabe D. *Crystal Plasticity Finite Element Methods In Materials Science and Engineering.* Weinheim, Germany: John Wiley & Sons; 2011.
32. Bažant ZP. Microplane model for strain-controlled inelastic behaviour. In: Desai CS, Gallagher R, eds. *Mechanics of Engineering Materials.* Hoboken, NJ: John Wiley & Sons; 1984:45-59.
33. Stroud AH. *Approximate Calculation of Multiple Integrals.* Upper Saddle River, NJ: Prentice-Hall; 1971.
34. Bažant ZP, Oh B. Efficient numerical integration on the surface of a sphere. *ZAMM-J Appl Math Mech/Z Angew Math Mech.* 1986;66(1):37-49.
35. Koiter WT. General theorems for elastic plastic solids. *Progress Solid Mech.* 1960;1:167-221.
36. Simo J, Kennedy J, Govindjee S. Non-smooth multisurface plasticity and viscoplasticity. loading/unloading conditions and numerical algorithms. *Int J Numer Methods Eng.* 1988;26(10):2161-2185.
37. Phillips A, Gray GA. Experimental investigation of corners in the yield surface. *J Basic Eng.* 1961;83(2):275-288.
38. Phillips A. On rate-independent continuum theories of graphite and their experimental verification. *Nucl Eng Des.* 1972;18(2):203-211.
39. Ashby M. The deformation of plastically non-homogeneous materials. *Philos Mag J Theoret Exp Appl Phys.* 1970;21(170):399-424.
40. Caner FC, Bažant ZP. Microplane model m7 for plain concrete. I: formulation. *J Eng Mech.* 2013;139(12):1714-1723.
41. Nguyen H, Pathirage M, Rezaei M, Issa M, Cusatis G, Bažant ZP. New perspective of fracture mechanics inspired by gap test with crack-parallel compression. *Proc Natl Acad Sci.* 2020;117(25):14015-14020.
42. Nguyen HT, Pathirage M, Cusatis G, Bažant ZP. Gap test of crack-parallel stress effect on quasibrittle fracture and its consequences. *J Appl Mech.* 2020;87(7):071012-1-071012-11.
43. Barenblatt G. Equilibrium cracks formed in a brittle fracture (in Russian). *Dokl Ak N.* 1959;127:47-50.
44. Xu X-P, Needleman A. Numerical simulations of fast crack growth in brittle solids. *J Mech Phys Solids.* 1994;42(9):1397-1434.
45. Bažant ZP, Planas J. *Fracture and Size Effect in Concrete and Other Quasibrittle Materials, New Directions in Civil Engineering.* Boca Raton, FL and New York, NY: CRC Press; 1998.
46. Moës N, Dolbow J, Belytschko T. A finite element method for crack growth without remeshing. *Int J Numer Methods Eng.* 1999;46(1):131-150.
47. Kirane K, Salviato M, Bažant ZP. Microplane triad model for simple and accurate prediction of orthotropic elastic constants of woven fabric composites. *J Compos Mater.* 2016;50(9):1247-1260.

48. Kirane K, Bažant ZP. Microplane damage model for fatigue of quasibrittle materials: sub-critical crack growth lifetime and residual strength. *Int J Fatigue*. 2015;70:93-105.
49. Li F, Li Z. Continuum damage mechanics based modeling of fiber reinforced concrete in tension. *Int J Solids Struct*. 2001;38(5):777-793.
50. van Mier JG. Multiaxial strain-softening of concrete. *Mater Struct*. 1986;19(3):190-200.
51. Bažant ZP, Cedolin L. *Stability of Structures: Elastic, Inelastic, Fracture and Damage Theories*. Hackensack, NJ: World Scientific; 2010.
52. Caner FC, Bažant ZP, Červenka J. Vertex effect in strain-softening concrete at rotating principal axes. *J Eng Mech*. 2002;128(1):24-33.
53. Budiansky B. *A Reassessment of Deformation Theories of Plasticity Technical Report*. Cambridge, MA: Harvard University; 1958.
54. Hutchinson J. Elastic-plastic behaviour of polycrystalline metals and composites. *Proc Royal Soc Lond Math Phys Sci*. 1970;319(1537):247-272.
55. Hutchinson JW. Plastic buckling. *Advances in Applied Mechanics*. Vol 14. Amsterdam, Netherlands: Elsevier; 1974:67-144.
56. Hecker S. *Experimental Studies of Yield Phenomena in Biaxially Loaded Metals., Technical Report*. Los Alamos, NM: Los Alamos Scientific Lab; 1976.
57. Bažant ZP. Endochronic inelasticity and incremental plasticity. *Int J Solids Struct*. 1978;14(9):691-714.
58. Hutchinson J, Neale K. Sheet necking-II. time-independent behavior. *Mechanics of Sheet Metal Forming*. New York, NY: Springer; 1978:127-153.
59. Christoffersen J, Hutchinson JW. A class of phenomenological corner theories of plasticity. *J Mech Phys Solids*. 1979;27(5-6):465-487.
60. Bažant ZP. Work inequalities for plastic fracturing materials. *Int J Solids Struct*. 1980;16(10):873-901.
61. Sinha BP, Gerstle KH, Tulin LG. Stress-strain relations for concrete under cyclic loading. *J Am Concr Inst*. 1964;61(2):195-212.
62. Nooru-Mohamed MB. *Mixed-Mode Fracture of Concrete: An Experimental Approach* [Ph. D. thesis]. Technische Universiteit. 1992.
63. Rudnicki JW, Chen C-H. Stabilization of rapid frictional slip on a weakening fault by dilatant hardening. *J Geophys Res*. 1988;93(B5):4745-4757.
64. Bažant Z, Pfeiffer P. Shear fracture tests of concrete. *Mater Struct*. 1986;192):111-121.
65. Griffith A. The phenomena of rupture and flow in solid, philosophical translation. *Royal Soc Lond Ser A Volucella*. 1921;221:582-593.
66. Barenblatt GI. The mathematical theory of equilibrium cracks in brittle fracture. *Adv Appl Mech*. 1962;7(1):55-129.

How to cite this article: Nguyen HT, Caner FC, Bažant ZP. Conversion of explicit microplane model with boundaries to a constitutive subroutine for implicit finite element programs. *Int J Numer Methods Eng*. 2020;1-15.
<https://doi.org/10.1002/nme.6590>